

A MULTI-MODALITY FIBER OPTIC SENSING CABLE FOR MONITORING ENHANCED GEOTHERMAL SYSTEMS

Sabarni Palit, William Challener, James Lopez, Sudeep Mandal, Hua Xia
GE Research
One Research Circle
Niskayuna, NY, 12309, U.S.A.
e-mail: challene@ge.com

Roger Jones, Russell Craddock, Li Zhao, and Muhammad Irshad
GE Sensing
Fir Tree Lane
Groby, Leicestershire, LE6 0FH, U.K.

Trevor W. MacDougall and Paul Sanders
QOREX, LLC
101 Hammer Mill Road
Rocky Hill, CT, 06067, U.S.A.

Brian Herbst, Brett Villiger
AFL
150 Ridgeview Circle
Duncan, SC 29334, U.S.A

Sonny Vo
420 Via Palou
Stanford University
Stanford, CA 94305, USA

Joseph Henfling, Scott Lindblom, Frank Maldonado
Sandia National Laboratories 1515 Eubank SE
Albuquerque, NM 87123

ABSTRACT

A suite of optical sensors for monitoring pressure and temperature in enhanced geothermal systems is being developed by a multidisciplinary team of researchers from GE, QOREX LLC, AFL Telecommunications and Sandia National Labs. In the second year of this DOE-sponsored project, a fiber optic cable and key sensing subsystems have been fabricated and tested in the laboratory for temperature and pressure response and accuracy, reliability and survivability at temperatures up to 400 °C and for hydrogen darkening of the fiber at high temperature and pressure.

Four different resonant MEMS sensors for point pressure measurements have been designed and fabricated for operation, in EGS environments with an optical fiber connection. Resonant frequencies vary between ~15 kHz and 90 kHz depending on sensor design, and laboratory measurements yielded sensitivities of frequency variation with external pressure of 0.9-2.2 Hz/psi. Linear performance was

verified at temperatures up to 100 °C. An FPGA-based optoelectronic feedback system for these sensors was also implemented and validated. A comprehensive survey of the specialty fiber supply chain led to procurement of a set of candidate high temperature, hydrogen-tolerant fibers that were evaluated for mechanical and hydrogen performance. Both multimode and single mode fibers have been qualified with polyimide and metal coatings. An FBG sensor for distributed pressure sensing has been designed for temperatures up to 400 °C and is being fabricated. The accuracy of a Raman distributed temperature sensing instrument has been demonstrated for use with pure silica core fiber even when the fiber exhibits differential fiber attenuation from a nominal amount of reversible hydrogen darkening. Results of the open and closed loop pressure sensing measurements, temperature dependence, manufacturing tolerance, and initial downhole field tests are described.

FIBER OPTIC SENSING SYSTEM FOR ENHANCED GEOTHERMAL SYSTEMS-OVERVIEW

The accurate sensing of temperature and pressure in the harsh environment of an enhanced geothermal system is both a need and a challenge. High temperatures (374 C) and pressures (220 bar) need robust sensor and package design. In the research described herein, a suite of fiber optic sensors for measuring temperature, pressure and strain are being integrated into a single cable for downhole utilization with the aim of making measurements in wells that may be up to 10 km deep. The desired pressure measurement accuracy is <1% for a desired lifetime of at least six months.

In the second year of this DOE-funded \$2.6M program, fiber capable of handling high temperatures and pressures has been evaluated for tensile strength and hydrogen-induced fiber attenuation.

A MEMs (microelectromechanical system)-based resonant pressure sensor, to be placed at the end of the fiber cable, has been designed and the first generation die have been tested under laboratory conditions.

Fiber Bragg grating (FBG) temperature and pressure sensor packages are being built and evaluated for use as distributed sensors in a single mode fiber. The FBG temperature sensor is particularly useful for correcting for the temperature response of both the MEMs pressure sensor and the FBG pressure sensor. A distributed temperature measurement is also being accomplished by a Raman system through a graded index multimode fiber. Brillouin measurements for distributed temperature and strain in a single mode step index fiber are also being implemented.

GE Global Research and GE Sensing are designing, fabricating and testing the MEMs and FBG pressure sensors for the program. QOREX has identified fibers suitable for EGS systems, selected suitable Raman DTS and BOTDR systems, incorporated a patented turnaround device at the bottom of the cable for the Raman DTS, and also verified that their compensation algorithm calibrates out effects of hydrogen-induced darkening. QOREX has worked with AFL to design the cable for the downhole test. The cable was constructed by AFL and the downhole testing is being supervised by Sandia National Laboratories.

MEMS POINT PRESSURE SENSOR

MEMs devices have been used in a variety of pressure sensing applications and are commercially available from GE, Honeywell, Freescale, Bosch, and

Motorola among others. For a harsh geothermal environment, where high temperatures and EMI may preclude the use of electronic sensors, an optically driven and interrogated highly accurate MEMs pressure sensor is especially attractive. A schematic of the pressure sensing scheme is shown in Fig. 1.

Laser light from both a “drive” laser and a “read” laser is conveyed to the sensor via a single optical fiber using a wavelength division multiplexer. The drive laser at a wavelength of 1310 nm is modulated by the output of a network analyzer. An area of the Si MEMs structure is heavily doped and thereby absorbs this wavelength, causing the Si resonator to be displaced by thermal expansion. When the drive is modulated at the correct frequency, the resonance is excited. A Fabry Perot cavity is formed between the Si cap over the MEMs chip and the MEMs resonator itself. The cavity size varies due to the vibrating resonator, and causes the reflected light from the continuous read laser to be modulated at the resonator frequency. The detected signal is then displayed by the network analyzer as the frequency is swept across the sensor resonant frequency band. The resonant frequency, resonance linewidth or “Q”, signal amplitude, and background noise level can be directly measured.

The sensor has also been operated without a network analyzer by means of a closed feedback loop. As shown in Fig. 1, the output of the detector is amplified and delayed through an FPGA. The signal is then fed back to the drive laser, enabling the system to oscillate around the resonant frequency of the MEMs device. The time delay is adjusted so that the feedback signal is in phase with the resonator to give the maximum signal amplitude.

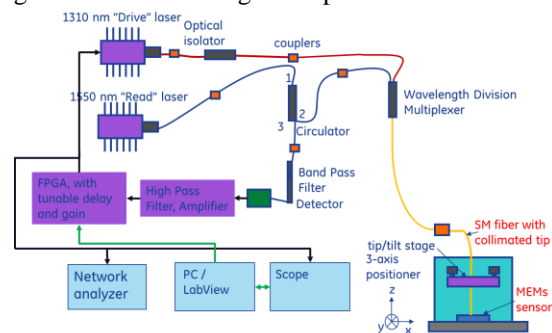


Fig. 1: Optically driven and interrogated Silicon MEMs point pressure sensor with feedback electronics.

Finite element analysis was carried out to design four different structures for the MEMs point pressure sensor that would be suitable for drive and interrogation through a single optical fiber attached to the chip. These designs are all based on an existing resonator type which was originally designed for electrostatic drive and capacitive interrogation. An

example is shown in Fig. 2. Of these, three of the sensors have been successfully characterized for open loop optical drive and read operation using a single single-mode (SM) fiber. Additionally, pressure and temperature response data have been collected on two of the designs and are reported here.

The modulation response of these sensors is a function of both the power and wavelength of the read laser. Varying the optical power of the laser not only changes the amount of heat delivered to the resonator, which may slightly change its resonant frequency, but also causes a shift in laser wavelength. A simple model of a plane wave incident upon a cavity formed by a 500 μm Si cap, a $\sim 20 \mu\text{m}$ vacuum gap, and a Si resonator exhibits reflectance variations with wavelength and vacuum gap distance as shown in Fig. 3. Consequentially, it is also important to measure the effect of the read laser current and wavelength on the signal.

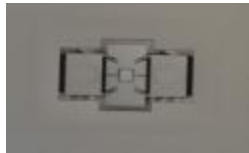


Fig. 2: Four resonator designs that have been fabricated: SEM image of GE's existing butterfly structure based resonant pressure transducer (RPT) currently used in electrostatically actuated pressure sensors, and tested for optical drive and read.

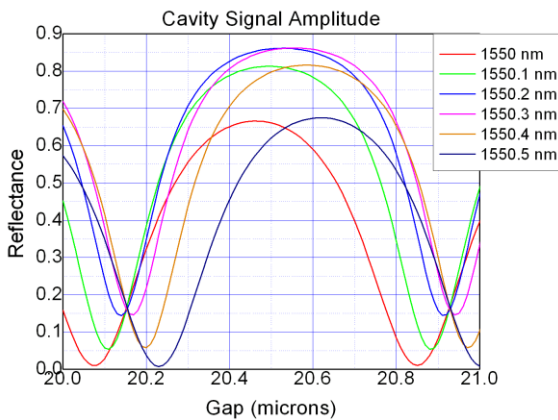


Fig. 3: Reflectance for a plane wave incident from a glass substrate onto a 500 μm Si cap, a 20 μm vacuum gap, and a Si resonator. Small changes in wavelength can cause large changes in operating point on the reflectance curve.

Two Beam MEMS Sensor Design

The first mode (fundamental frequency) of the two beam resonator design occurs at ~ 13 kHz, and the third at ~ 92 kHz. The latter mode is designed to have

the highest Q factor, although both modes were studied in this experiment. The second mode could not be observed for this configuration, probably because this mode has a zero displacement node at the resonator - fiber coupling point, and thus cannot be optically excited.

The pressure sensitivity of the two beam sensor was measured at various chip temperatures. To vary the chip temperature, a resistive heater was placed below a copper plate on which the sensor was mounted. Figs. 4(a) and (b) show the measured data and linear fits of the resonant frequency as a function of pressure at 24, 50, 75 and 100 C for the first and third resonant modes, respectively. In all cases, the sensor shows a linear response. The slope of these plots represents the pressure sensitivity of the two beam sensor at these different temperatures, and this is shown in Fig. 5(a). The third resonant mode of the sensor is found to be approximately 1.4 times more sensitive than the first resonant mode. Fig. 5(b) shows the effect of chip temperature on resonant frequency at ambient pressure. This results in a temperature sensitivity of -3.5 Hz/psi for the third mode and -1 Hz/psi for the first.

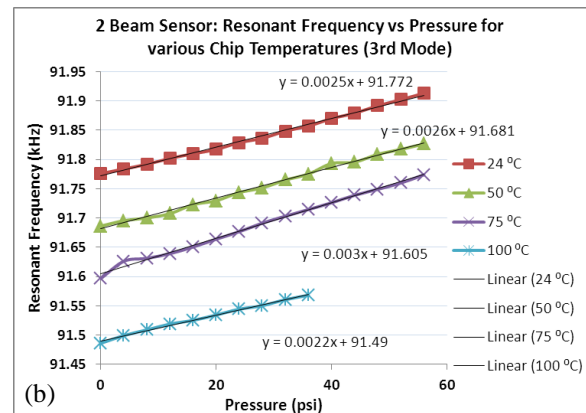
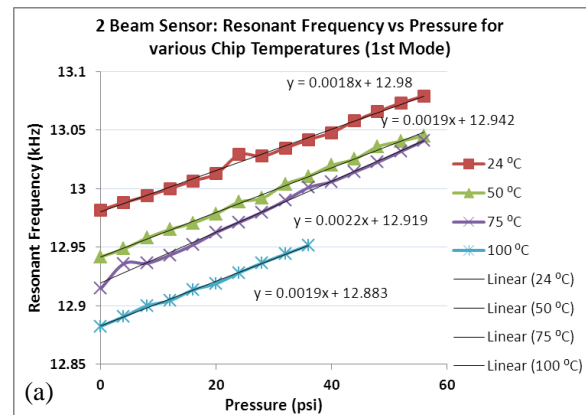


Fig. 4: Plot of resonant frequency as a function of pressure for 2 beam sensor at 24, 50, 75 and 100 C for (a) first resonant mode (b) third resonant mode.

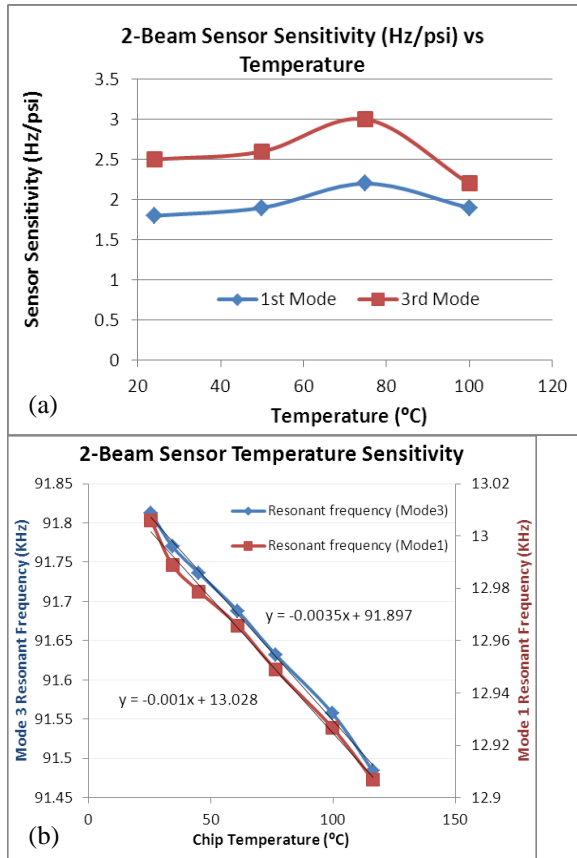


Fig. 5: (a) Pressure sensitivity (slope of plots in Fig. 4(a) and (b)) of the 2 beam sensor vs. chip temperature. The pressure sensitivity varies between 1.8 to 2.2 Hz/psi for the 1st resonant mode and 2.2 to 3 Hz/psi for the 3rd resonant mode. (b) Temperature sensitivity of the 2-beam sensor at atmospheric pressure.

Four Beam MEMS Sensor Design

For the four beam MEMS sensor, the readback signal power was found to peak at a read laser temperature of 26 C corresponding to a wavelength of 1559.5 nm, and a drive current of 200 mA, hence this setting was used for all subsequent pressure measurements. This was with an RF power of 9 dBm for a drive laser current of 200 mA, corresponding to 14.76 mW optical power incident on the sensor, at 20 C.

The pressure sensitivity of the 4-beam sensor was measured at various chip temperatures. Chip temperature was set by means of a thermoelectric cooler (TEC), enabling more accurate and stable temperature profiles. However, the greatest source of error was the limited resolution of the pressure gauge on the pressure vessel. Measurements were further complicated by a slow leak of the vessel. Fig. 6 (a) shows measured data and linear fits of the resonant frequency as a function of pressure at 25, 40, 60, 80 and 100 C. Measurements repeated at 25 C and 40 C

(not shown), resulted in slopes between 0.7 and 1.3 Hz/psi. The sensor cap thickness was chosen to reduce the pressure sensitivity by about two orders of magnitude from a commercially available electrostatically-actuated MEMS sensor design. For this project, the desired pressure range is 220 bars, corresponding to 3200 psi. Therefore, there should be ~3 kHz frequency shift from the initial resonance at ~18 kHz. Our pressure vessel for measurements on unpackaged sensors is only suitable for a maximum pressure of 50 psi, but packaged sensors can be tested to > 2000 psi in the laboratory.

In Fig. 6(b) the resonant frequency was captured at a constant pressure but the temperature was varied. The temperature sensitivity is -1.1 Hz/C, which is within the error margin of the value of -0.9Hz/ C calculated from the y-intercepts of the linear fits in Fig. 6(a). The temperature sensitivity is about the same as mode 1 of the two-beam sensor and one third that of mode 3 of the two-beam sensor.

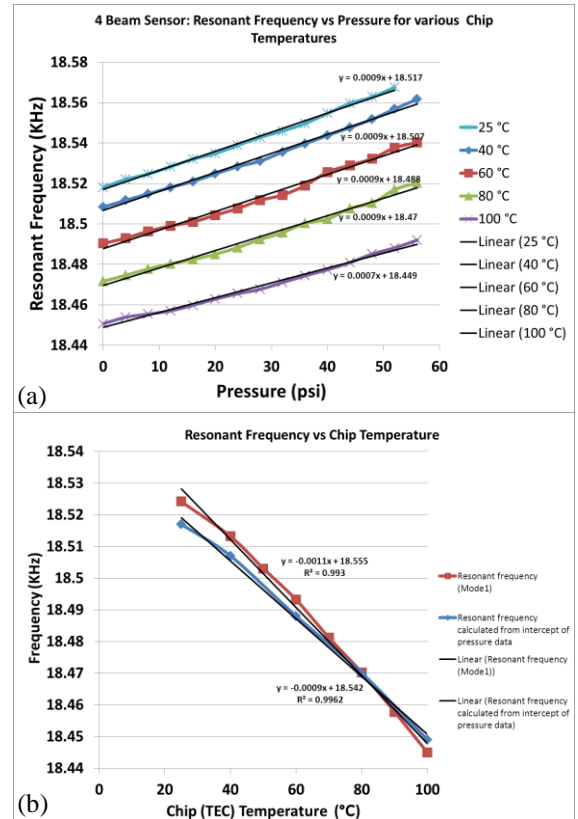


Fig. 6: (a) Plot of resonant frequency as a function of ambient pressure for the 4-beam sensor at 25, 40, 60, 80 and 100 C. The slopes indicate pressure sensitivities of 0.7 to 0.9 Hz/psi. (b) Resonant frequency as a function of chip temperature for the 4-beam sensor at ambient pressure (red), and calculated from y-intercepts of (a) (blue).

Fiber To MEMs Alignment Tolerance

A critical aspect of the packaged MEMS sensor is the coupling of the fiber to the MEMS chip, and tolerances associated with the alignment of the fiber to the sensor. Manufacturing tolerances dictate that sensor should work with the fiber being within $\pm 100 \mu\text{m}$ lateral distance of the optimum coupling point on the chip, and with a vertical fiber-to-chip gap that may vary between 0 and $300 \mu\text{m}$, with a maximum limit of $500 \mu\text{m}$.

The lateral sensitivity of the fiber coupling to the 2-beam sensor was estimated by aligning and adjusting its tilt to get the maximum peak power. This point corresponds to the origin (i.e., $x=0, y=0$) in Fig. 7. Subsequent scans were conducted by moving the fiber along two orthogonal directions (axes of the translation stage on which the fiber was mounted) in the plane of the sensor as shown in Figs. 7 (a) and (b). Along the x-axis, translation of the fiber over $80\text{--}100 \mu\text{m}$ still resulted in a reasonably strong peak signal power. Along the y-axis, the fiber could be translated approximately $40 \mu\text{m}$ ($20 \mu\text{m}$ on each side of the origin) while maintaining reasonably high peak signal powers.

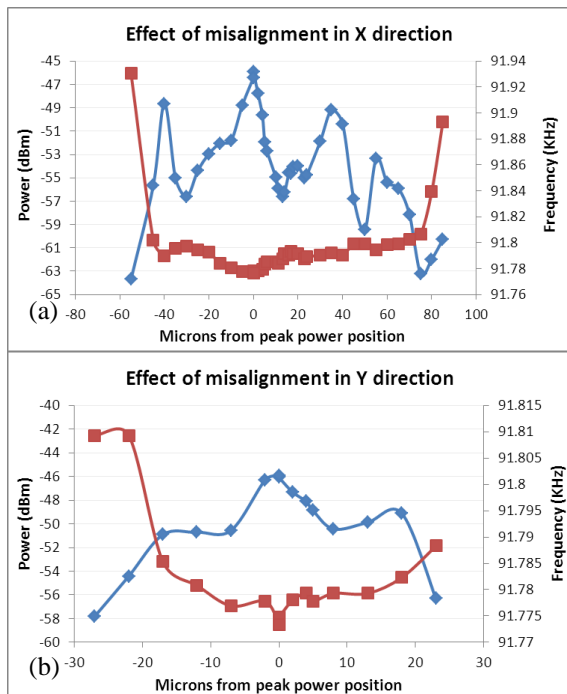


Fig. 7: Lateral sensitivity of two beam sensor: Effect on power and frequency when scanning the optical fiber along the (a) X-direction and (b) Y-direction.

The lateral sensitivity of the four-beam sensor was estimated by finding the alignment of the fiber at which the peak power was maximum and then scanning to the left, right, up and down from this

point, as was done for the two-beam sensor. It was possible to scan in one of the directions for $90\text{--}250 \mu\text{m}$, depending on the particular die being tested. Large signal variations observed in the scan along the perpendicular direction result from a feature in the resonator design that can be eliminated in future die.

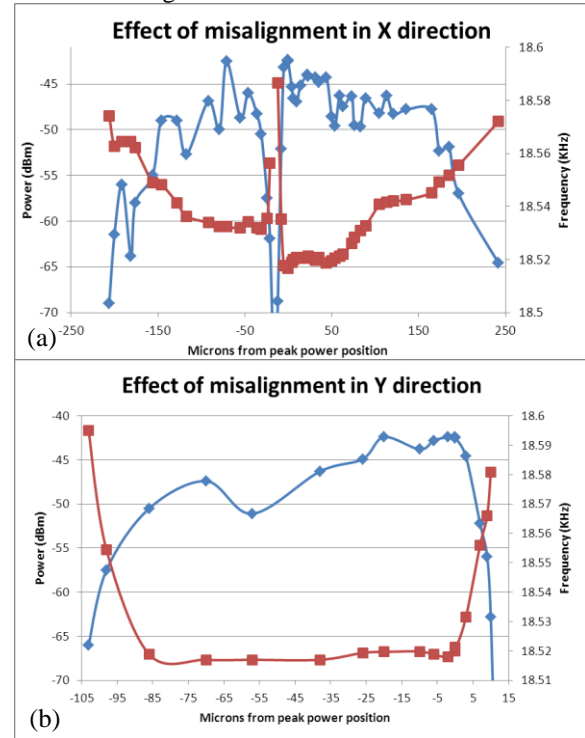


Fig. 8: Lateral sensitivity of four beam sensor: Effect on power and frequency when scanning the optical fiber along the (a) x-direction and (b) y-direction of the 4-beam sensor.

As manufacturing tolerances can cause a separation of as much as $300 \mu\text{m}$ between the fiber tip and sensor, the two-beam and four-beam sensors were tested with flat cleaved and collimated single-mode (SM) fiber tips.

Fig. 9 (a) and (b) show the vertical sensitivity of the readback signal using a cleaved SM fiber for the third mode of a two-beam sensor and the fundamental mode of a four-beam sensor, respectively. Commercially available index matching fluid with an index of 1.69 was used with the two-beam sensor, while a high temperature oil that will be incorporated in the packaged sensors with a refractive index of 1.54 at a wavelength of 589.29 nm was used with the four-beam sensor. In both cases, the fiber could be pulled away from the sensor by up to $300 \mu\text{m}$ before the signal merged with the noise floor in a 30 Hz bandwidth. Fig. 9(c) illustrates measurements for a four-beam sensor using a collimating fiber tip in air. The initial SNR of 30 dB in a 30 Hz bandwidth was maintained as the fiber was separated up to $1000 \mu\text{m}$ from the sensor surface. It was found that the signal

variation was less sensitive to fiber tilt for the collimating fiber than for the cleaved fiber.

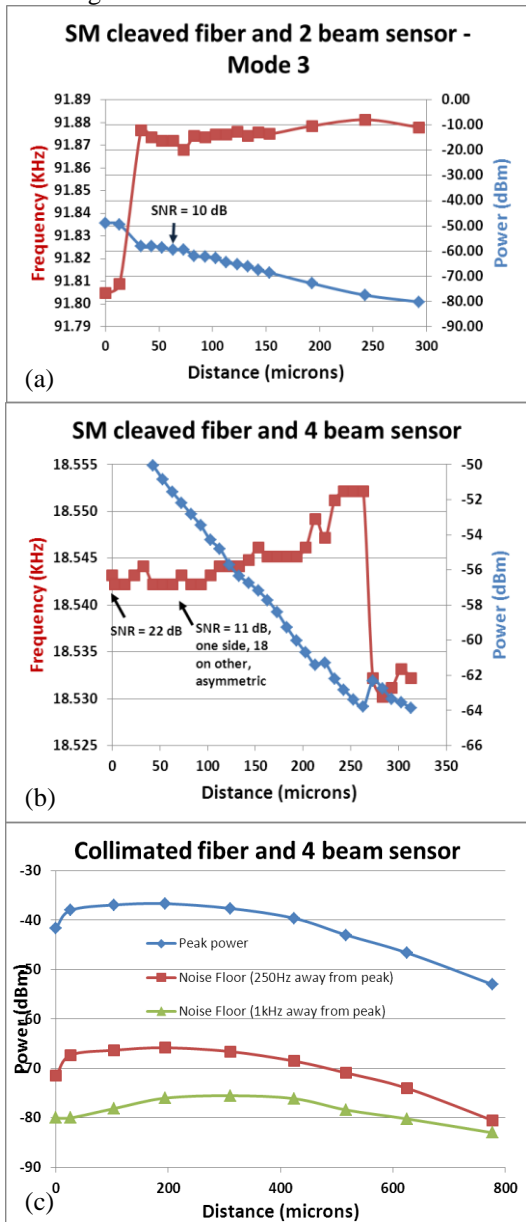


Fig. 9: Effect of separation between fiber and sensor on peak power and resonant frequency for (a) SM cleaved fiber and 2 beam sensor (b) SM cleaved fiber and 4 beam sensor and (c) SM collimated tip fiber and 4 beam sensor.

Feedback Loop

After testing various four-beam sensor dies, one with a high SNR (sample 4BB3 from the previous section) was chosen for a closed feedback loop experiment. For the four-beam sensor experiment, a hardware closed loop setup was assembled as shown in Fig. 1, and the phase of the amplified detected signal was varied through an FPGA-based delay block, before the signal was fed back to modulate the drive laser.

Fig. 10 shows the spectrum of the signal from the network analyzer and the corresponding oscilloscope trace as the phase was varied.

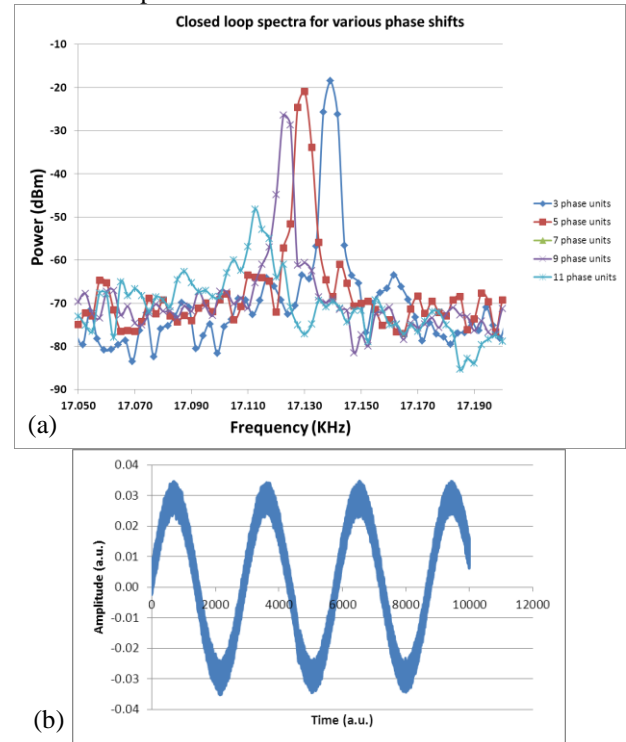


Fig. 10 (a). Spectrum of detected signal for 4 beam sensor run in closed loop (b) Oscilloscope trace of the detected signal.

The pressure sensitivity of the sensor was measured in closed loop at ambient temperature, as shown in Fig. 11, resulting in a sensitivity value of 1.2 Hz/psi, which is again within the margin of error of the value 0.9 Hz/psi measured in open loop.

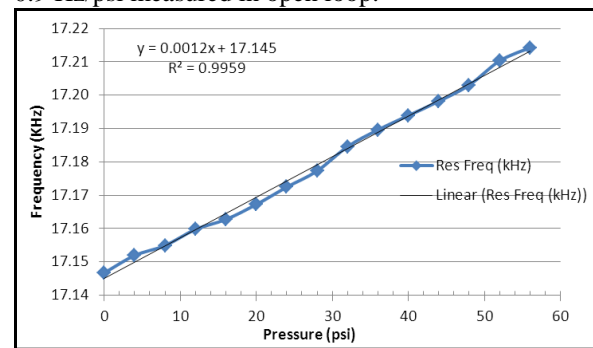


Fig 11: Resonant frequency versus pressure, at ambient temperature for 4 beam sensor in closed loop.

The optical attenuation expected from a fiber cable that is several kilometers long was simulated by inserting an attenuator in the WDM coupler path before the sensor. The optical attenuation could then be increased until the feedback loop was no longer able to track the sensor resonance. With the noise sources in the present system, at least 4.5 mW of

drive laser power and 6 mW read laser power injected into the fiber cable were required for closed loop operation. In our optical system, the drive laser has a maximum output power of 100 mW and the read laser has a maximum output power of 80 mW, so there is a substantial margin available to overcome any attenuation of the lasers in the fiber cable.

MEMS Sensor Package For EGS Environment

The silicon MEMS chip must be protected from the EGS environment to obtain a sufficient lifetime. It is, therefore, packaged in an Inconel 625 housing fitted with a flexible Inconel diaphragm. The pressure of the EGR fluid is transmitted through the diaphragm to the chip by means of a silicone oil fill. The fiber is brazed into a ferrule, which interfaces with the Inconel housing and positions the end face of the fiber with respect to the MEMS chip as shown in the figure.

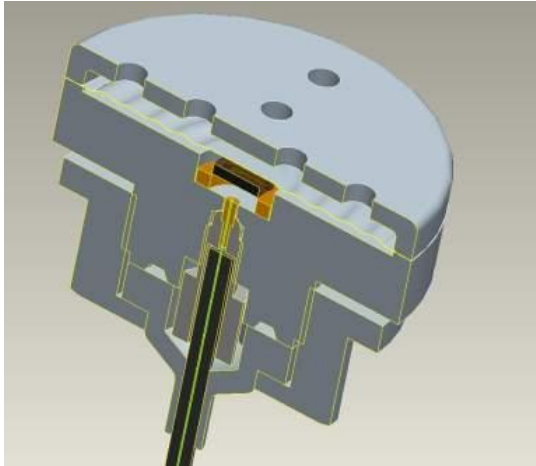


Fig. 12: Cross section of Inconel based package for MEMS pressure sensor

Care needs to be taken in the package design to allow for the differences in thermal expansion between Inconel, silicon and glass fiber to ensure that the necessary alignment tolerances are maintained over the full temperature range.

DISTRIBUTED TEMPERATURE AND PRESSURE SENSORS

Raman and Brillouin-based sensing systems have been used for temperature and strain measurements in enhanced geothermal systems, and form a part of the suite of sensors being developed for this project as well. In addition, a quasi-distributed fiber Bragg grating (FBG) sensor is also being developed for multi-point pressure and temperature measurements.

Raman DTS

As laser light propagates in an optical fiber, inelastic scattering with the molecular structure of the glass produces light at both a lower energy (wavelength

up-shifted or Stokes line) and a higher energy (anti-Stokes line). In Raman DTS systems, the relative intensity of these lines is a function of the local temperature in the fiber where the light scattering takes place. A temperature profile all along the fiber can be calculated by injecting light pulses into the fiber and measuring the return time and intensity of the Stokes and anti-Stokes Raman lines. The simplicity of this effect has led to predominance of Raman DTS systems as a powerful downhole monitoring and well logging tool in oil and gas.

The main challenge to be addressed for measurements in enhanced geothermal systems is that hydrogen diffusion into the sensing fiber can create wavelength-dependent differential fiber attenuation (DFA). This effect can cause the relative intensities of the Stokes and anti-Stokes lines to vary and thereby corrupt the temperature measurement. The effect of DFA can be compensated by using two fibers in the cable that are joined at the bottom by a turnaround loop. A compensation algorithm based on the differences in estimated temperature from two common depth points on the loop distance can then be applied to the Raman data to back out the effect of hydrogen darkening and calculate the correct temperature.

QOREX has developed a compact waveguide device to provide the turnaround at the bottom of the fiber loop, and a proprietary hydrogen compensation algorithm capable of producing accurate temperature measurements by calibrating out not only the effect of hydrogen darkening, but also other DFA sources, over a wider temperature range.

A commercial Raman DTS instrument produced by AP Sensing was selected for this program. The unit features a rugged, hermetically sealed optoelectronics module, with a pump laser that stimulates Raman backscatter signals at wavelengths less prone to hydrogen absorption effects in the fiber. The Raman DTS data acquisition module includes the AP Sensing instrument, an optical switching unit for injecting laser light into either end of the fiber loop, and an electronics processor to operate the dual-ended DTS measurement protocol and compensation algorithm.

Evaluation of compensated and non-compensated DTS measurements was performed on samples of conventional fiber and hydrogen-tolerant polyimide-coated fibers installed serially in a hydrogen test cell at 500 psi pure hydrogen at 270 C. As shown in Fig. 13, in-situ data for standard single-ended DTS and for dual-ended/compensated measurements were compared. The temperature calculated from single-ended measurements resulted in a 100 C offset from the chamber controller temperature, while the

compensated DTS measurement was in excellent agreement with the controller temperature.

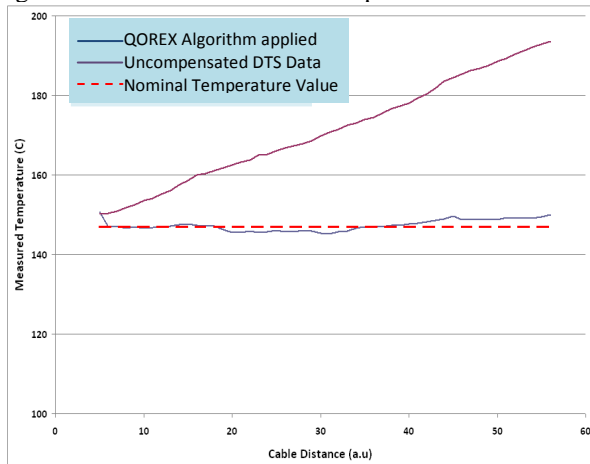


Fig. 13: Raman DTS: Experimental comparison of single ended DTS with dual ended/compensated system.

Commercial Brillouin DTSS

Brillouin backscattering produces both temperature and strain sensitive frequency shifts due to interaction with vibrational modes in the fiber. In Brillouin distributed temperature and strain sensors (DTSS), the frequency analysis of the Brillouin spectrum is complemented with amplitude analysis to compensate the cross-sensitivity. As with Raman DTS, a pulsed time domain measuring system is used to provide distributed temperature and strain measurements along the sensing fiber. In oil and gas, temperature is used to model flow and other well operations, with strain used to monitor parameters such as casing integrity. The added complexity in discriminating between measurands with Brillouin technology has retarded commercial adoption compared to Raman DTS systems.

By contrast, emerging applications for Brillouin DTSS in long reach, high temperature, and hydrogen rich environments such as EGS can leverage its inherent advantages in frequency-encoded measurement that is not affected by hydrogen induced DFA, allowing sensing fiber to be installed single-ended. This may ultimately reduce cost compared to Raman systems that require dual-ended architectures in high temperature wells. Further advantages in operating on single mode fiber include longer reach and immunity to modal and other error sources that affect Raman DTS systems.

QOREX conducted a formal review of existing commercial Brillouin systems. The QOREX turnaround device can also be extended for single mode fibers to operate a Brillouin Optical Time Delay Analysis (BOTDA) system over single-fiber Brillouin OTDR. Review of Brillouin systems

included strain sensitivity, spatial resolution, and thermal measurement performance comparison to Raman DTS technology. BOTDA specifications provided by the suppliers showed optimum performance, but in many cases involve a mix of fibers to achieve this performance or discriminate between strain and temperature. In contrast, BOTDR, which operates on a single fiber, offers suitable thermal measurement performance in terms of accuracy and resolution, and while falling short of the strain resolution achievable with BOTDA, such level of performance is likely beyond that required in the EGS application. Narrowing the selection to BOTDR showed some products not fully refined for such single-fiber BOTDR operation. Among suppliers, the Yokogawa unit has been in the commercial stream the longest based solely on the BOTDR approach, and was selected for this program.

Fiber Bragg Grating-Based Pressure Sensor

Fiber Bragg gratings (FBGs) inscribed in single-mode optical fibers can be packaged to sense temperature and pressure, either as single-point sensors or as sensing arrays. FBGs are written directly into the fiber core, causing a strong reflection peak over a narrow bandwidth of about 0.2 nm. Light from a broadband source or tunable laser is reflected from the grating when its wavelength satisfies the Bragg resonant condition. The Bragg resonant wavelength of a grating, λ_B , is determined by a unique grating period Λ , such that $\lambda_B = 2 \cdot n \cdot \Lambda$, where n is the effective refractive index of the fiber core. Multiple FBGs can be cascaded in a single fiber, each corresponding to a unique wavelength reflected from a certain distance in the fiber, as shown in Fig. 14. The wavelength shifts when the effective refractive index or the grating period changes due to temperature or strain. An array of these FBGs on a fiber, each with a unique Bragg resonant wavelength can be used to estimate temperature and/or strain along the length of the fiber either using wavelength/frequency division multiplexing or time division multiplexing technology.

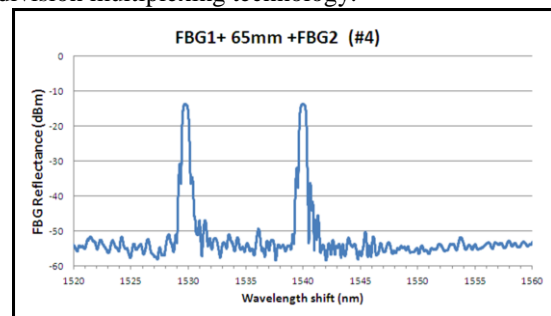


Fig. 14: Reflectance spectra of two fiber Bragg gratings with different Bragg wavelengths cascaded (spliced) onto the same single mode fiber 65 mm apart.

In order to measure distributed pressure, a package must be designed to transduce pressure into strain. The program goals of 220 bar and 374 C necessitate the use of a metal clad fiber enclosed in a hermetically-sealed package. Two fibers and a differential measurement that separates the effects of thermal expansion from strain are necessary. A temperature measurement is obtained from a free standing FBG. A measurement sensitive to both temperature and strain (or pressure) is obtained from a second FBG. Preliminary results for a FBG pressure sensor were reported in Ref. 1. The effect of strain on the FBG was quantified, and linearity and the need for a hermetical package and bonding material that minimizes thermal strain were ascertained.

We have tested the temperature stability for fiber Bragg gratings written in metalized SM fiber for 1600 hours. Fibers were coated with Cu, Al or Au. Three of the fibers exhibited a satisfactory long term drift after a 72 hour anneal at 400 C. One of the copper-coated fibers, however, exhibited a larger drift and strain from thermal compression. Specifically, when cooled back to room temperature, the FBG failed.

A bonding adhesive was identified that achieved 10,000 μ strain at high temperature, sufficient for bonding the fiber to the metallic package in spite of differential thermal expansion. This Al-cladded SM fiber with a patterned FBG was integrated into a bellow structure package with the high temperature adhesive, as shown in Fig. 15.

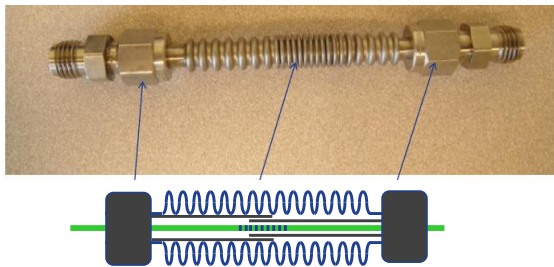


Fig. 15. FBG-based pressure sensor prototype-I with a stainless steel bellow structure.

The results of testing the prototype FBG-based pressure sensor prototype-I, as shown in Fig 16, indicated that there was probably a permanent deformation of the sensor package because the zero level at the end of the experiment did not go back to the initial level for either fiber. Moreover, changes in the zero level at intermediate steps indicated that there was a loss of hermeticity in the seal.

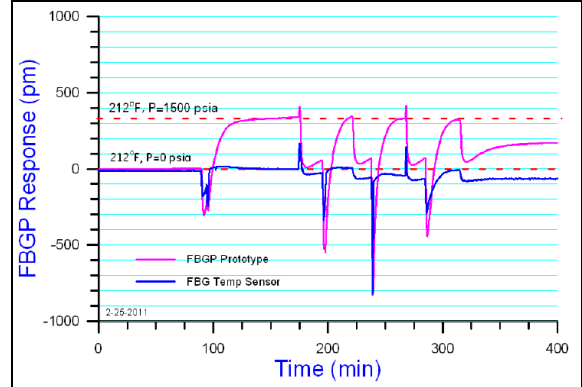


Fig 16: Change in FBG peak wavelength as a function of time as the external pressure on the sensor was varied between 0 psia and 1500 psia. The magenta curve is for the fiber designed to measure both pressure and temperature while the blue curve is for the fiber designed to measure just temperature.

The prototype-I FBG-based pressure package was modified to better transduce pressure into fiber strain without causing irreversible deformation of the package. This was implemented in this device by not relying on the elasticity of the bellows itself for reversibility, but rather making use of the external spring around the bellows. The prototype-II pressure sensor package is shown in Fig. 17. The external spring is designed to ensure that the package returns to its initial state after the pressure is released. As such, the spring strength can be adjusted for the desired pressure range of the sensor.



Fig. 17: Second generation FBG sensor package.

The sensor was tested in the laboratory by repeatedly cycling it between low and high pressures. Results from two sets of measurements, one for cycling from ambient to high pressure, and the other for ambient to low pressure as shown in Fig. 18 (a) and (b) respectively, indicates that the Bragg wavelength tracks the pressure.

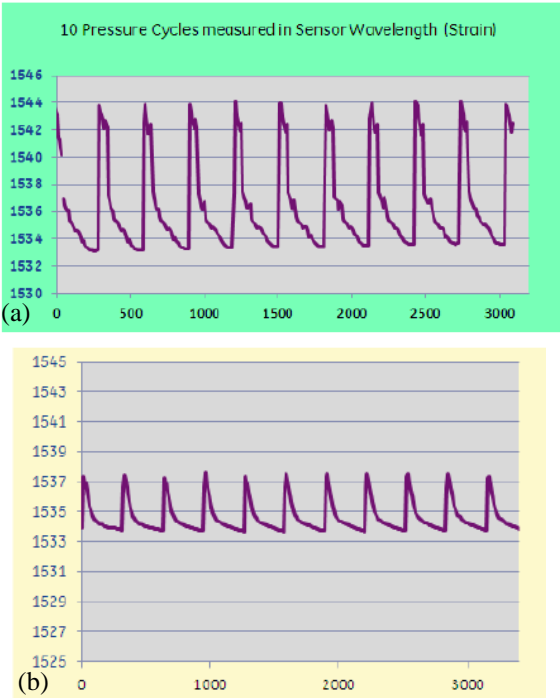


Fig. 18: Variation in wavelength of FBG-based prototype-II pressure sensor as the pressure is repeatedly cycled (a) from ambient to high pressure, and (b) from ambient to a lower pressure.

The initial positive results of this test indicate that it is suitable for further extensive testing of repetitive cycling at elevated temperatures and pressures. Prior to integration within a fiber cable, an outer package will also need to be integrated onto the sensor. This package will also have to ensure a hermetic seal between the fiber and fiber package.

For the first downhole test, we have integrated the FBG temperature sensor (required for differential measurements, as discussed earlier) within the fiber cable. The FBG sensor was annealed at 250 C to remove residual stress, and then interrogated. Fig. 19 shows the reflectance spectrum, indicating a Bragg wavelength of 1538.15 nm after the thermal annealing process mentioned above. A closeup, as shown in Fig. 19(b), illustrates the exact shape of the spectrum (red line), which is fairly flat at the peak, and has a secondary lobe. After the fiber was spliced and integrated in the cable for the downhole test, the spectrum was obtained again (blue line – shifted up by 10 dB). While the shape remained the same, the overall reflectance was lower, as expected due to connector and splicing losses.

The temperature sensitivity of the Al-clad FBG sensors was verified by taking two of these sensors through a series of temperature steps concurrently with a precision resistance thermometer up to 250 C at ambient pressure.

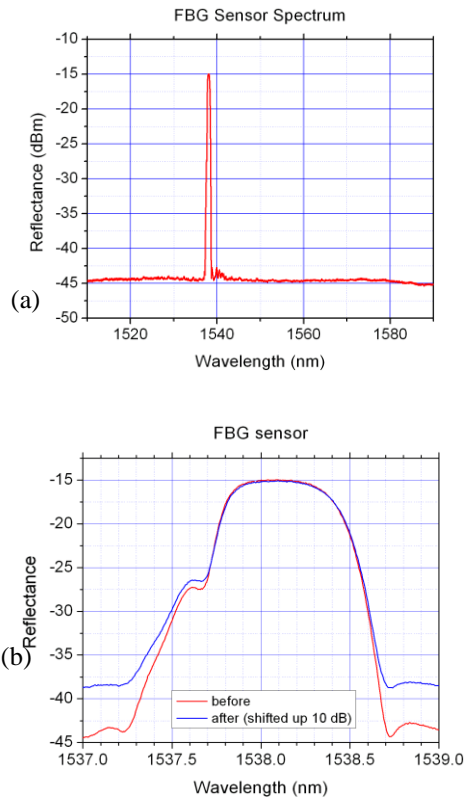


Fig. 19: (a) Reflectance spectrum from Al clad FBG sensor after annealing (b) Close-up of reflectance spectrum after annealing, and after incorporation into cable.

The conversion from change in Bragg wavelength $\Delta\lambda$ to temperature was performed by fitting a cubic polynomial of $\Delta\lambda$ to obtain T. A look up table has been generated for field tests with an accuracy of < 1 C over this temperature range.

In principle, however, the Al-clad FBG allows a maximum temperature of 400 C.

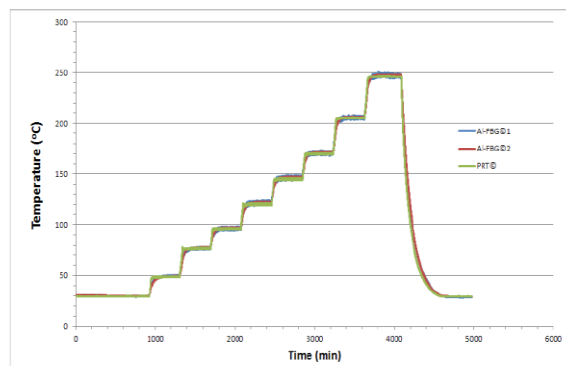


Fig. 20. Fiber sensor calibration with precision resistance thermometer. Red and blue plots are for the Al-clad FBG and back up FBG sensor. The PRT plot (green line) is concurrent with these plots.

FIBER OPTIC CABLE

The optical fiber for an EGS environment needs to be able to handle high temperatures in a hydrogen-rich environment. Repeated thermal cycling also dictates the need for a low strain cable design. Such cables are currently used in thermal recovery and in the oil and gas sector, and are being leveraged for this project.

Optical Fiber

As reported in Ref. 1, commercially available single and multimode fibers were evaluated, with all-silica cores for resisting hydrogen darkening, and polyimide and metal coatings for withstanding high temperatures. Two temperature ratings were considered: 300 C, which enables operability in a majority of the EGS resources, and 374 C for the specific targets of this program. Of the fibers shown in Table 1, five fibers have been identified by QOREX based on mechanical strain testing. Metallized MM fibers of type “I” and “K”, and SM fiber of type “L” were found to perform adequately up to 400 C, while polyimide-coated MM fibers “A” and “D” and SM fibers “E” and “H” were adequate to 300 C.

Table 1: Candidate fibers for down hole tests.

Fiber	Waveguide	Coating	Rating
A	50/125 MM Step-Index Pure Silica Core	Polyimide	300°C
D	50/125 MM Graded-Index Synthetic Silica	Polyimide	300°C
E	9/125 SM Step-Index Synthetic Silica	Polyimide	300°C
H	9/125 SM Step-Index Pure Silica Core	Polyimide	300°C
I	50/125 MM Step-Index Pure Silica Core	Aluminum	400°C
K	50/125 MM Step-Index	Aluminum	400°C
L	9/125 SM Step-Index Pure Silica Core	Aluminum	400°C

Hydrogen-induced attenuation was also tested for these fibers. The attenuation was too low to be measured for the metallized fibers up to 300 C. However, the glass composition and waveguide design of the metallized fibers are identical to those of the qualified polyimide-coated fibers, i.e., they use the same glass preform and should exhibit similar hydrogen performance in the absence of the metallized coating. Fig. 21 shows the relative

transmission of Fibers “A” and “D” at an elevated temperature, as a function of distance.

Two test fibers and a control fiber are spliced together. Due to the high loss that the Ge-doped control fiber has when exposed to hydrogen, it is placed at the end of the spliced fiber train. The fiber is loaded into the test chamber, brought up to the test temperature of ~210 C and allowed to stabilize for about 4 hrs. Nitrogen pressure is then applied to mechanically set and stabilize the fiber, followed by a settling time of two hours, after which the temperature-induced effects and mechanical effects have stabilized and the effects of hydrogen can be isolated. The baseline plot is the data after stabilization and prior to any hydrogen exposure. The hydrogen is introduced into the chamber, diffusing into the core of the fibers very quickly at this temp (~5 min). A Raman DTS system is used to indicate relative optical attenuation at intervals of 125 hrs and 250 hrs. Following these measurements, the hydrogen atmosphere is removed. Hydrogen diffuses out of the core glass very quickly. After a one hour delay, another Raman measurement determines any irreversible effects from the hydrogen. The overlap of the cyan curve with the purple curve for fibers “A” and “D” indicate no irreversible hydrogen darkening, while the large difference between these curves for the conventional control fiber indicates that it has suffered severe irreversible hydrogen darkening.

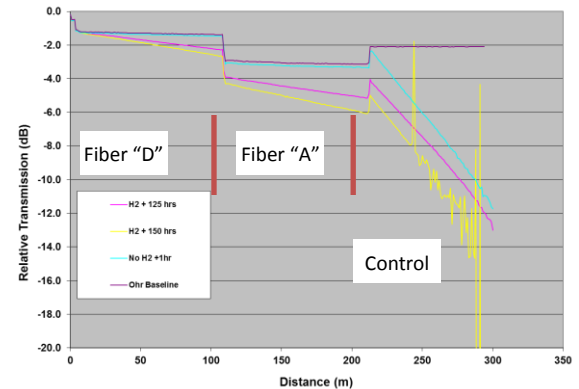


Fig. 21. Optical characterization of all-silica core fibers “D” and “A” indicated no impact of reversible hydrogen darkening.

Cable

The fiber optic cable for an EGS environment needs to be able to handle high temperature, corrosive environment and the rigors of installation. The cable structure consists of an outer ¼” metal tube that utilizes Incoloy™ 825 material with a wall thickness of 0.035”. Incoloy 825 is commonly used for fiber optic and “TEC”, tube encapsulated copper, instrumentation cables for downhole monitoring in the oil and gas sector. This material is used where H₂S- hydrogen sulfide, or high CO₂ –carbon dioxide, levels exist such that corrosion is a concern. The

wall thickness of the tube is selected based on the pressure in the well, the type of completion and the desired ruggedness to account for upsets during installation. For more severe environments, a 0.049" wall thickness could be used.

Inside the 1/4" tube, is a stainless steel tube that houses the selected fibers – two 50 μm graded index multimode fibers with a carbon polyimide coating and one pure silica core single mode with a polyimide coating. The optical fibers are pulled into the stainless steel tube making process in such a way that they are not exposed to the laser welding process which seals the tube. One of the key design parameters for the stainless steel tube manufacturing is to ensure that there is adequate excess fiber in the tube to keep the optical fibers from being exposed to strain in the target environment. Fiber strain can lead to increased attenuation, termination difficulties, contamination of certain fiber optic sensing technologies, or worse, broken fibers. Mechanical and thermal strain must be considered when determining the appropriate level of excess fiber. Through AFL's proprietary methods, excess fiber can be incorporated into the design to keep the fiber strain free up to the designed temperature limit of the cable.

To characterize the proposed cable, a series of mechanical tests were performed:

1. Stress/Strain Test
2. Crush Test
3. Impact Test
4. Installation or Sheave Test

The purpose of the Stress/Strain Test is to tension the cable while monitoring cable strain, tension, fiber strain and fiber attenuation. The single mode fiber was used for monitoring fiber strain while the 50 μm multimode fibers were monitored for attenuation. The cable tension was increased in 75 lb increments up to 2000 lbs. At the 2000 lb level, the cable strain was 0.39%. The average optical attenuation increase from baseline on the two 50 μm multimode fibers at this level was 0.01%. The designed excess fiber length exceeded the cable strain at this level ensuring a strain free fiber in deployment.

The purpose of a Crush Test is to determine the level of deformation of the cable with a defined load and to characterize the optical loss on the optical fibers under such load. The test method used for guidance was TIA/EIA-455-41A, Crush Test. The cable is located between two metal plates that are 100 mm long on which the crush load is applied. The optical fibers are monitored for a change in optical loss during the testing. The starting load was 909 kg or 2000 lbs. After each test, the cable was shifted 150 mm to a new location and the load increased by 455

kg. At each test location, the deformation in the tube and the optical loss on the fibers were recorded. The first point of deformation occurred at 1818 kg or 4000 lbs with tube deformation measuring 0.04 mm. There was no incremental optical loss at this level. The balance of the test is shown in Fig. 22. Note that the fibers did not break up through the final measurement. At 5000 kg, the optical loss on one fiber jumped notably but dropped back to baseline for the balance of the test. This can be explained as the optical fiber undergoing a microbend during the application of the force such that the optical loss increased, but once the load was removed, the microbend was relieved. Note that although the optical loss results are low throughout most of the test, the cable was severely compromised at ~2700 kg and would be considered unusable.

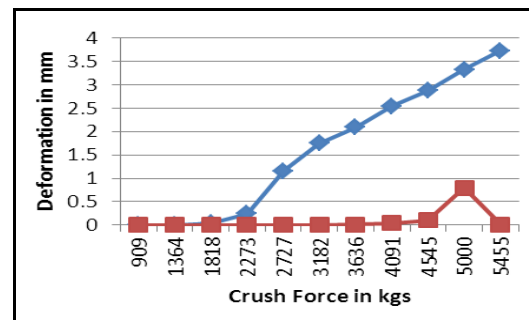


Fig. 22: Crush test on optical cable indicating deformation (blue) and optical loss (red).

The purpose of the Impact Test is to characterize the effect on the cable from an impact load. The test method used for guidance was TIA/EIA 455-25C, Impact Test. The point of contact on the cable is a rounded metal semi-circle with a radius of 25 mm. The weight is dropped from a height of 150 mm with the striking surface perpendicular to the cable. The weights used for this test were 5 kg, 10 kg and 15 kg, translating to a test impact energy of 7.3 N*m, 14.6 N*m and 21.9 N*m. At each level, deformation and optical loss were recorded. Two impacts were completed at three locations at each level of impact energy. Fig. 23 captures the results of the tests showing the highest deformation and optical loss at each level. There was essentially no optical loss throughout the test on any of the three fibers. At the conclusion of the test, the number of impacts was increased until at least one fiber broke. At 10 impacts with a weight of 15 kg, one of the multimode fibers broke – the other two fibers had no optical loss at this point.

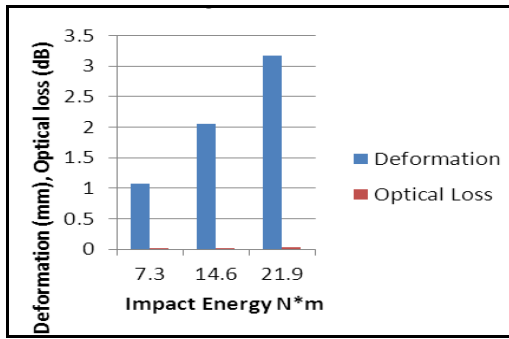


Fig. 23: Impact test on optical cable. No optical loss is seen until the fibers break.

The Installation or Sheave Test is intended to characterize the effects on a cable, both mechanical and optical, during installation. The cable is passed over a sheave under load multiple times while attenuation is being monitored on each of the optical fibers. Cable deformation during the test is also captured through measurement with a caliper. For this test, the cable was passed over a 16" sheave with a 13" root diameter at a 30° angle with a tension of 177 kg, which is ~15% of the rated breaking strength of the cable. The cable is cycled back and forth over the sheave under tension fifteen times. The results of the test were no change in optical performance on single mode or on the two multimode fibers throughout the test. Subsequently, and during the test, the cable was measured at three locations for deformation. The deflection from nominal was a maximum of 0.01 mm or 0.0004" at all three locations. This level of ovality is still within the workable tolerance for compression fittings so there should not be any detrimental impact to cable installation at this level.

FIRST DOWNHOLE TEST

The first downhole test of the fiber optic cable began on December 14, 2011, lasting about four weeks. The cable was inserted into a geothermal well in Nevada owned by Ormat as shown in Fig. 24. The well is an observation well with a depth of ~5000 feet. The well was first logged and then the cable insertion was completed satisfactorily over two days. Continuity of the fiber was tested both prior to insertion, when the cable had been partially inserted, and finally after full insertion.



Fig. 24: Ormat geothermal observation well with fiber cable installed. The opposite end of the cable on the spool is attached to the measurement instruments inside the trailer via a fiber extension cable. The instruments can be operated either from a solar power panel on top of the trailer or a gasoline generator.

The cable was inserted to a depth of 4500 feet to avoid a potential obstruction noted during the logging at 4700 feet. Raman DTS and FBG temperature sensor readings were collected at well depths of 1000 feet and 4500 feet during and immediately after insertion, and then periodic measurements were planned throughout the remainder of the test. Normalized FBG spectra from the sensor at room temperature and at the two well depths are shown in Fig. 25.

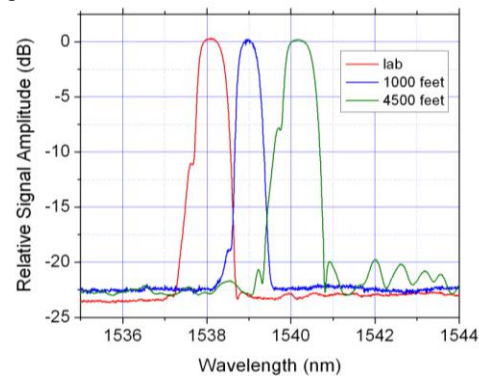


Fig. 25: FBG spectra measured in the lab at 20 C, and then at 1000 feet and 4500 feet during cable insertion. The differences in shape of the spectra are due to a different Micron Optics instrument used to collect spectra during the well test than the during the initial lab measurements. Also, the channel 1 input on the instrument was used for the 1000 foot measurement, but stopped working thereafter, so the channel 2 input was used for subsequent measurements at 4500 feet.

Unfortunately, the spectral shape of these three measurements varies due to two reasons. The Micron Optics instrument used in the lab to calibrate the sensor was not available for the downhole test, so a different unit was used instead for the measurements at 1000 and 4500 feet. Moreover, channel 1 of the second unit was used for the spectrum at 1000 feet, but then this channel failed, so all subsequent downhole measurements were made using channel 2 of the instrument.

Using the laboratory FBG calibration to convert the spectral measurements to temperatures gave results that were ~19 C greater than those obtained from the well log performed prior to the cable insertion at a depth of 1000 ft, and ~42 C at a depth of 4500 ft. Although this may be in part related to the different Micron instrument used to measure the spectra, it also probably indicates that the FBG fiber has suffered some strain during the process of well insertion. After the cable has been removed from the well at the end of the test, further measurements in the lab of the FBG spectra will be used to diagnose the change in spectral shape and temperature calibration. The FBG fiber was placed loosely within the terminating section of the cable where the MM fiber return loop was located, but was not otherwise protected from bending. Therefore, during the next test of this sensor, it will be placed within its own metal tube to further protect it from any external strain.

Data collected from the sensor over the initial five day period after insertion indicated essentially no change in temperature at the bottom of the well, as expected, and as shown in Fig. 26.

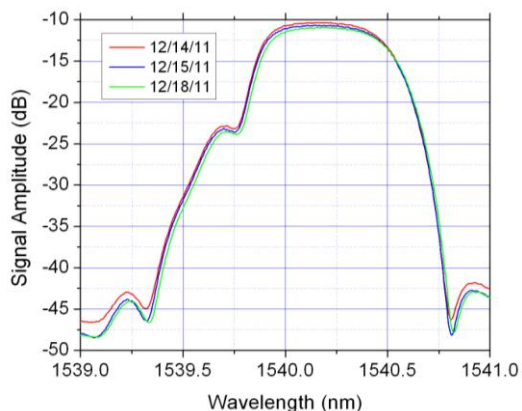


Fig. 26: FBG spectra measured at a well depth of 4500 feet spanning a five day period after insertion of the cable in the well.

Raman DTS and Brillouin OTDR measurements were also performed on the installed cable. Preliminary results, prior to calibration of the Brillouin data for strain effects, are shown in Fig. 27

and are consistent with the initial well log. In particular, at 1000 feet (305 m), the measured temperature is 107 C and at 4500 feet (1370 m) the measured temperature is 200 C.

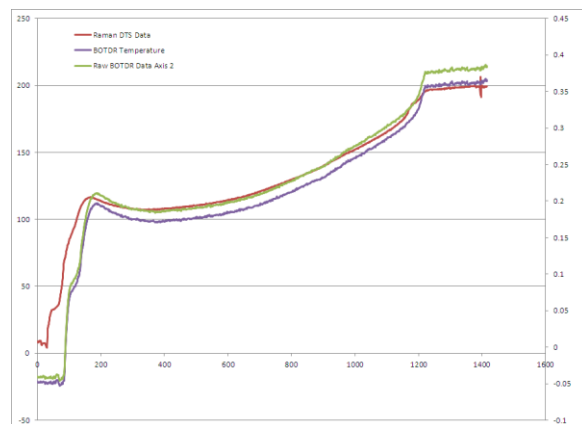


Fig. 27. (red) Raman DTS temperature results. (purple) Brillouin OTDR temperature results. (olive) Brillouin OTDR raw data (right scale).

CONCLUSION

Progress towards the development of a multi-mode fiber optic sensing cable for enhanced geothermal systems has been reported. Optical fiber which satisfactorily resists hydrogen darkening and which maintains its tensile strength at high temperatures has been identified. Two MM fibers and one SM fiber have been incorporated into a fiber cable, along with a FBG temperature sensor and a MM fiber loop at the bottom of the cable. The cable has been successfully inserted into a geothermal observation well and initial measurements of FBG spectra and Raman DTS and Brillouin OTDR have been made successfully. Further results will be obtained over the course of the four week test.

In addition, progress has been made towards developing a highly accurate MEMS point pressure sensor. Several new MEMS sensor designs have been fabricated and tested in the lab at low pressures. Alignment tolerances have been measured. An optical fiber interrogation system using two lasers and a single SM optical fiber has been demonstrated in the lab. A feedback loop for sensor measurements has also been designed and demonstrated.

A second downhole test of the fiber cable is expected as part of this project for later in the spring of 2012 which will test the MEMS pressure sensor, along with possibly an FBG pressure/temperature sensor and a Rayleigh COTDR distributed temperature sensor. The results of the first test are expected to lead to several improvements for the second test.

ACKNOWLEDGEMENTS AND DISCLAIMER

We are grateful to Ormat Technologies for providing a geothermal well site to test the cable and sensors, and to Stephanie Konefat of Ormat for her help in many ways during the cable installation.

This material is based upon work supported by the Department of Energy-Golden Field Office under Award DE-EE0002787.

This report was prepared as an account of work sponsored by an agency of the United States government. Neither the United States government nor any agency thereof, nor any of their employees, makes any warranty, express or implied, or assumes any legal liability or responsibility for the accuracy, completeness, or usefulness of any information, apparatus, product, or process disclosed, or represents that its use would not infringe privately owned rights. Reference herein to any specific commercial product, process, or service by trade name, trademark, manufacturer or otherwise does not necessarily constitute or imply its endorsement, recommendation, or favoring by the United States government or any agency thereof. The views and opinions of authors expressed herein do not necessarily state or reflect those of the United States government or any agency thereof.

REFERENCES

1. W. Challener, A. Knobloch, M. Ajgaonkar, P. Chamarthy, H. Xia, R. Jones, R. Craddock, L. Zhao, P. Kinnell, T. W. MacDougall and P. Sanders, "Subsystem design and validation for optical systems for monitoring enhanced geothermal systems," [*Proc. 36th Workshop Geotherm. Res. Eng.*](#) (2011) SGP-TR-191.